Publ. Astron. Soc. Japan (2020) 72 (2), 33 (1–18)
doi: 10.1093/pasj/psaa009
Advance Access Publication Date: 2020 February 12

Deeply cooled core of the Phoenix galaxy cluster imaged by ALMA with the Sunyaev–Zel'dovich effect

Tetsu Kitayama,[1,*] Shutaro Ueda,[2] Takuya Akahori,[3] Eiichiro Komatsu,[4,5] Ryohei Kawabe,[6,7,8] Kotaro Kohno,[9,10] Shigehisa Takakuwa,[11] Motokazu Takizawa,[12] Takahiro Tsutsumi,[13] and Kohji Yoshikawa[14]

[1]Department of Physics, Toho University, 2-2-1 Miyama, Funabashi, Chiba 274-8510, Japan
[2]Academia Sinica Institute of Astronomy and Astrophysics (ASIAA), No. 1, Section 4, Roosevelt Road, Taipei 10617, Taiwan
[3]Mizusawa VLBI observatory, National Astronomical Observatory of Japan, 2-21-1 Osawa, Mitaka, Tokyo 181-8588, Japan
[4]Max-Planck-Institut für Astrophysik, Karl-Schwarzschild Strasse 1, D-85741 Garching, Germany
[5]Kavli Institute for the Physics and Mathematics of the Universe (Kavli IPMU, WPI), Todai Institutes for Advanced Study, The University of Tokyo, 5-1-5 Kashiwanoha, Chiba 277-8583, Japan
[6]National Astronomical Observatory of Japan, 2-21-1 Osawa, Mitaka, Tokyo 181-8588, Japan
[7]The Graduate University for Advanced Studies (SOKENDAI), 2-21-1 Osawa, Mitaka, Tokyo 181-8588, Japan
[8]Department of Astronomy, The University of Tokyo, 7-3-1 Hongo, Bunkyo, Tokyo 113-0033, Japan
[9]Institute of Astronomy, School of Science, The University of Tokyo, 2-21-1 Osawa, Mitaka, Tokyo 181-0015, Japan
[10]Research Center for the Early Universe, School of Science, The University of Tokyo, 7-3-1 Hongo, Bunkyo, Tokyo 113-0033, Japan
[11]Department of Physics and Astronomy, Graduate School of Science and Engineering, Kagoshima University, 1-21-35 Korimoto, Kagoshima, Kagoshima 890-0065, Japan
[12]Department of Physics, Yamagata University, 1-4-12 Kojirakawa-machi, Yamagata, Yamagata 990-8560, Japan
[13]National Radio Astronomy Observatory, P.O. Box 0, Socorro, NM 87801, USA
[14]Center for Computational Sciences, University of Tsukuba, 1-1-1 Tennodai, Tsukuba, Ibaraki 305-8577, Japan

*E-mail: kitayama@ph.sci.toho-u.ac.jp

Received 2019 November 22; Accepted 2020 January 29

Abstract

We present measurements of the thermal Sunyaev–Zel'dovich effect (SZE) toward SPT-CL J2334−4243 (the Phoenix galaxy cluster) at $z = 0.597$ by the Atacama Large Millimeter/submillimeter Array (ALMA) in Band 3. The SZE is imaged at 5″ resolution (corresponding to the physical scale of 23 h^{-1} kpc) within 200 h^{-1} kpc from the central galaxy, with the peak signal-to-noise ratio exceeding 11. Combined with the Chandra X-ray image, the ALMA SZE data further allow for non-parametric deprojection of electron temperature, density, and entropy. Our method can minimize contamination by the central active galactic nucleus and the X-ray absorbing gas within the cluster, both of

© The Author(s) 2020. Published by Oxford University Press on behalf of the Astronomical Society of Japan. This is an Open Access article distributed under the terms of the Creative Commons Attribution License (http://creativecommons.org/licenses/by/4.0/), which permits unrestricted reuse, distribution, and reproduction in any medium, provided the original work is properly cited.

Downloaded from https://academic.oup.com/pasj/article/72/2/33/5803376 by University of Tsukuba user on 07 October 2021

which greatly affect the X-ray spectrum. We find no significant asymmetry or disturbance in the SZE image within the current measurement errors. The detected SZE signal shows much higher central concentration than other distant galaxy clusters and agrees well with the average pressure profile of local cool-core clusters. Unlike in typical clusters at any redshift, the gas temperature drops by at least a factor of 5 toward the center. We identify $\sim 6 \times 10^{11}\ M_\odot$ cool gas with temperature $\sim$3 keV in the inner 20 h^{-1} kpc. Taken together, our results imply that the gas is indeed cooling efficiently and nearly isobarically down to this radius in the Phoenix cluster.

Key words: cosmology: observations — galaxies: clusters: individual (SPT-CLJ2344−4243) — galaxies: clusters: intracluster medium — radio continuum: galaxies — techniques: interferometric

1 Introduction

It has long been argued that the density of thermal gas particles in cores of galaxy clusters is large enough for these particles to cool radiatively, leading to a runaway "cooling flow" toward the cluster center (e.g., Fabian 1994 for review). Such rapid gas cooling or associated star formation in central galaxies, however, has not been observed in galaxy clusters in the local Universe. Radiative gas cooling must then be suppressed, e.g., by feedback from an active galactic nucleus (AGN) often hosted by a central galaxy (e.g., McNamara & Nulsen 2007; Fabian 2012), while the exact mechanism is yet uncertain.

The Phoenix galaxy cluster, SPT-CL J2344−4243, at redshift $z = 0.597$ possibly provides a unique counter example to suppressed gas cooling mentioned above. It is the most X-ray luminous galaxy cluster known to-date with exceptionally high concentration of thermal gas within the central 100 kpc; the predicted cooling (or mass deposition) rate amounts to $\dot{M}_{\rm cool} = 2000$–$4000\ M_\odot\ {\rm yr}^{-1}$ (McDonald et al. 2012, 2013; Ueda et al. 2013). The central galaxy of the Phoenix cluster is also unique in that its star formation rate $\dot{M}_{\rm SF} = 400$–$900\ M_\odot\ {\rm yr}^{-1}$ (McDonald et al. 2012, 2013; Mittal et al. 2017) is among the largest in any galaxy at $z < 1$, it hosts a dusty type II quasar (Ueda et al. 2013), and it is associated with extended filaments of warm ($\sim 10^4$ K) ionized gas (McDonald et al. 2014a) and cold molecular gas (Russell et al. 2017).

One of the key questions on the nature of the Phoenix cluster is how much thermal gas is in fact cooling to sufficiently low temperatures. While the presence of cool plasma with temperature $kT \lesssim 3$ keV, where k is the Boltzmann constant, has been reported in the literature (Ueda et al. 2013; Pinto et al. 2018; McDonald et al. 2019), the deposition rate of such gas is often inferred to be lower than the values quoted above (Tozzi et al. 2015; Pinto et al. 2018; McDonald et al. 2019). This may imply that radiative cooling is still suppressed at $kT > 3$ keV in this cluster. A major challenge in the X-ray analysis of this cluster is the presence of a bright AGN and possibly cold neutral gas in the central galaxy; the former dominates the X-ray emission at energies $E > 2$ keV and the latter modifies the spectrum at $E < 2$ keV via absorption (McDonald et al. 2019; see also subsection 4.1). It is hence crucial to explore the physical states of the gas by other independent methods.

In this paper, we report on measurements of the thermal Sunyaev–Zel'dovich effect (SZE: Sunyaev & Zel'dovich 1970, 1972) towards the Phoenix cluster by the Atacama Large Millimeter/submillimeter Array (ALMA). While the cluster was first identified via the SZE by the South Pole Telescope (SPT) (Carlstrom et al. 2011; Williamson et al. 2011), its internal structures were not explored because of the moderate angular resolution (>1′) of the SPT. We present the first spatially resolved SZE image of the Phoenix cluster at an angular resolution of 5″ using ALMA Band 3 (section 3). We further explore thermodynamic properties of the hot gas in conjunction with the X-ray data taken by Chandra (section 4). The high-resolution SZE image from ALMA provides an independent and complementary probe of the intracluster medium (ICM) to X-rays.

Throughout the paper, we adopt a standard set of cosmological density parameters, $\Omega_{\rm M} = 0.3$ and $\Omega_\Lambda = 0.7$. We use the dimensionless Hubble constant $h \equiv H_0/(100\ {\rm km\ s^{-1}\ Mpc^{-1}})$; given controversial results on the value of h (e.g., Verde et al. 2019) we do not fix it unless otherwise stated. In this cosmology, the angular size of 1″ corresponds to the physical size of 4.67 h^{-1} kpc at the source redshift $z = 0.597$. The errors are given in 1σ and the coordinates are given in J2000.0.

2 Observations and data reduction

SPT-CL J2344–4243 was observed by the 12 m and 7 m arrays of ALMA (project code: 2015.1.00894.S) as summarized in table 1. The observations were executed in four and 15 separate blocks for the 12 m and 7 m arrays, respectively. Each execution block lasted less than 80 minutes

Downloaded from https://academic.oup.com/pasj/article/72/2/33/5803376 by University of Tsukuba user on 07 October 2021

Table 1. Summary of observations.

Array	12 m	7 m
Date	2016 March 17–19	2016 May 3–June 12
Total on-source time [hr]	3.21	8.06
Number of execution blocks	4	15
Number of antennas	36–37	7–10
Flux calibrator	Neptune	Neptune, Uranus
Phase calibrator	J2336−4115	J2328−4035
Bandpass calibrator	J2357−5311	J0006−0623, J2258−2758, J0538−4405
Central frequency [GHz]	92	92
Band widths [GHz]	7.5	7.5
Baseline coverage [kλ]	3.7–145	2.1–15.6
Primary beam FWHM at the central frequency [″]	62	107
Number of pointings	7	7

Table 2. Properties of synthesized images.

Array	12 m	12 m (>30 kλ only)	7 m	12 m + 7 m
Beam major axis FWHM [″]	2.22	1.86	19.7	2.25
Beam minor axis FWHM [″]	1.89	1.61	11.5	1.92
Beam position angle [°]	76.6	74.4	84.2	76.6
Average 1σ noise [mJy beam^{-1}]	0.0123	0.0144	0.0714	0.0122

including overheads. The number of antennas and calibrators slightly varied among the execution blocks, as listed in table 1. All the data were taken at four continuum bands centered at 85, 87, 97, and 99 GHz, yielding an overall central frequency of 92 GHz with an effective bandwidth of 7.5 GHz. Compact configurations were adopted to cover the baseline ranges of 3.7–145 kλ and 2.1–15.6 kλ for the 12 m and 7 m arrays, respectively, where λ is the observed wavelength. They yielded the angular resolution and the maximum recoverable scale of ∼2″ and ∼60″, respectively.

The target field, centered at ($23^{\rm h}44^{\rm m}43\overset{\rm s}{.}90$, $-42^\circ43'12\overset{''}{.}00$), had a diameter of about $1\overset{'}{.}5$ covered with seven hexagonal mosaic pointings by both arrays. An equal spacing of $34\overset{''}{.}2$ between the pointings was adopted, yielding approximately the Nyquist sampling for the 12 m array and much denser sampling for the 7 m array.

Throughout this paper, we used the visibility data produced by the second stage of ALMA's Quality Assurance process (QA2). Imaging was done with the Common Astronomy Software Applications package (CASA: McMullin et al. 2007) version 5.6.1. The procedure was similar to that of Kitayama et al. (2016). We adopted the multi-frequency synthesis mode in joint mosaic imaging. Natural weighting was used and all the images presented were corrected for primary beam attenuation.

Table 2 lists the parameters of the synthesized beams as well as the 1σ noise levels of the synthesized image within 45″ from the field center. The noise levels were measured on a difference map created after subtracting the compact sources as described in subsection 3.1, dividing the data set in half, taking a difference between their dirty images, and dividing it by a factor of 2 to correct for the reduction of the integration time.

3 Results

3.1 Compact sources

There are four compact sources detected by emission above the 5σ significance level in our target field. As described below, we determined their positions and flux densities by fitting with the CASA task *uvmodelfit* the 12 m array visibility data at baselines longer than 30 kλ [corresponding to the spatial scale smaller than λ/(30 kλ) ∼7″] to eliminate contamination by the extended SZE. Source identification and subtraction are done in the *uv* plane and are fully independent of the image synthesis method. The results are summarized in table 3. These sources are also detected at 18 GHz by ATCA and their properties are discussed in detail in a separate paper (Akahori et al. 2019). The assigned source names are the same as in Akahori et al. (2019); C1, C2, and C3 are central sources in descending order of their 18 GHz flux, whereas W is a western off-center source.

The brightest central source, C1, is an AGN hosted by the central galaxy. Figure 1a shows a dirty image toward source C1 produced by the visibility data at >30 kλ. Throughout this paper, we denote the projected angular

Downloaded from https://academic.oup.com/pasj/article/72/2/33/5803376 by University of Tsukuba user on 07 October 2021

Table 3. Positions and flux densities of compact sources in the observing field.*

Source ID	Model	RA (J2000.0)	Dec (J2000.0)	92 GHz flux density [mJy]
C1	Point-like	$23^h44^m43^s.905$	$-42°43'12''.548$	1.891 ± 0.010
C2	Gaussian	$23^h44^m43^s.884$	$-42°43'10''.633$	0.090 ± 0.017
C2	Point-like	$23^h44^m43^s.887$	$-42°43'10''.684$	0.068 ± 0.010
C3	Point-like	$23^h44^m43^s.973$	$-42°43'13''.493$	0.091 ± 0.010
W	Point-like	$23^h44^m41^s.661$	$-42°43'22''.139$	0.158 ± 0.010

‡The errors in the positions are less than $0''.15$ and the effective angular resolution is $1''.86 \times 1''.61$ FWHMs (table 2). Sources C1, C3, and W are assumed to be point-like. Source C2 is modeled by an elliptical Gaussian (see text for details) but the results of a point source model fit are also shown for reference.

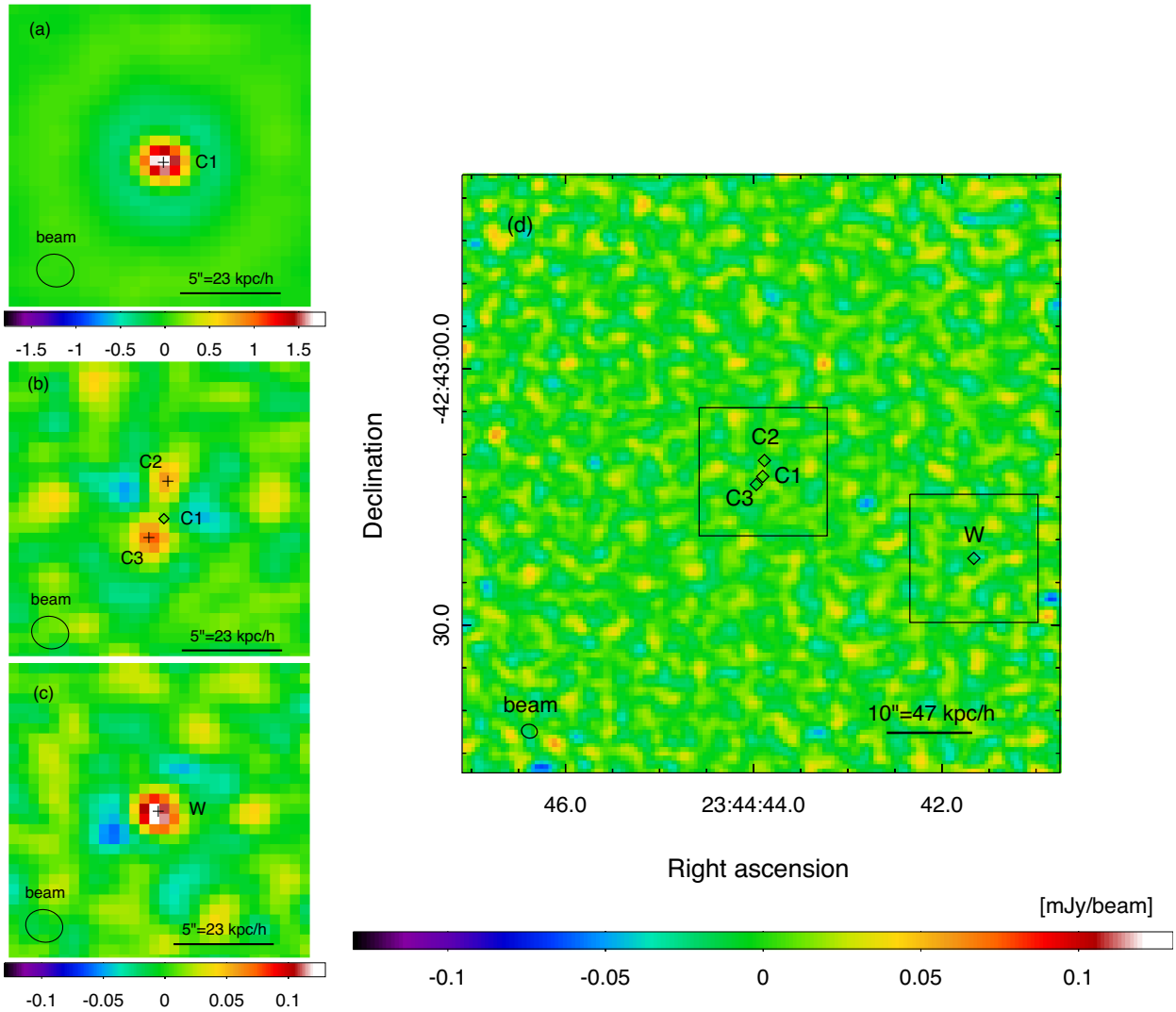

Fig. 1. Dirty images produced by long-baseline (>30 kλ) visibility data. Positions of identified sources before and after subtraction are marked by crosses and diamonds, respectively. The synthesized beam shape (table 2) is shown at the bottom left of each panel. (a) The central $15'' \times 15''$ region before the sources are subtracted. Sources C2 and C3 are not prominent because source C1 is much brighter. (b) Same as panel (a) but after source C1 is subtracted. (c) The region around source W. (d) The image after sources C1, C2, C3, and W are subtracted. Boxes indicate the regions shown in panels (a), (b), and (c). (Color online)

Downloaded from https://academic.oup.com/pasj/article/72/2/33/5803376 by University of Tsukuba user on 07 October 2021

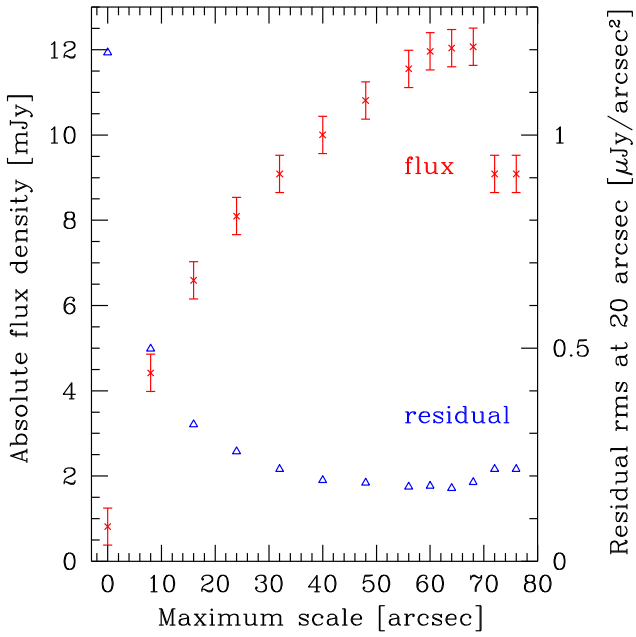

Fig. 2. Recovered flux and residuals within the field of view (1.′5 in diameter) versus the maximum scale of Gaussians used in Multi-Scale CLEAN. Wherever smaller than the scale shown in the figure, Gaussians with FWHMs of 0, 4″, 8″, 16″, and 32″ are also used in the deconvolution; the smaller scale values are fixed for comparison. The plotted residual is the rms value measured on a residual map after being corrected for primary beam attenuation and smoothed by a Gaussian kernel with 20″ FWHM. (Color online)

distance and the deprojected physical distance from source C1 by θ and r, respectively.

When the best-fitting point source model for source C1 (table 3) is subtracted from the visibility data, two weaker sources, C2 and C3, become apparent near the cluster center (figure 1b). In addition, there is another off-center source, W, at $\theta \sim 25''$ from the west of source C1 (figure 1c). As the shapes of sources C3 and W are consistent with the synthesized beam, they are modeled by point sources. We checked that the results in table 3 are essentially unchanged when these sources are modeled by a Gaussian varying its full width at half maximum (FWHM) as a free parameter. On the other hand, source C2 appears to be elongated from northwest to southeast. We thus modeled this source by an elliptical Gaussian, fixing the major-to-minor axis ratio at 0.05, to obtain the major axis FWHM of $1.''3 \pm 0.''5$ and the position angle of $-9.^\circ4 \pm 21.^\circ8$, with the centroid position and flux density listed in table 3. We checked that the results are insensitive to the assumed value of the axis ratio as long as the minor axis remains negligible compared to the synthesized beam size. For comparison, if source C2 is modeled by a point source, the fitted flux is lower by about 25% (table 3).

Figure 1d shows a long baseline (>30 kλ) image after all the detected sources are removed from the visibility data. The residuals have a root mean square (rms) value of 0.0146 mJy beam^{-1} and are consistent with noise. This confirms that identification and subtraction of the sources are properly done.

3.2 The Sunyaev–Zel'dovich effect

The source-subtracted visibility data were deconvolved with the Multi-Scale CLEAN algorithm (Cornwell 2008; Rich et al. 2008; Steeb & Rau 2019) using the CASA task *tclean*. We adopted [0, 4″, 8″, 16″, 32″, 64″] as the FWHMs of the Gaussian components used in Multi-Scale CLEAN implemented in CASA version 5.6.1.[1] As illustrated in figure 2, this is an optimal choice for the present target and assure maximal recovered flux as well as minimal residuals. We used a circular mask region with radius $\theta = 42''$, a flux threshold of 0.024 mJy, and a loop gain of 0.05.

Figure 3 shows the deconvolved SZE image created from the visibility data taken by the 12 m and 7 m arrays after the compact sources described in subsection 3.1 are removed. The image has been smoothed to an effective beam size of 5″ FWHM for display purposes; unless otherwise stated, quantitative analysis in this paper was done on the unsmoothed image with $2.''25 \times 1.''92$ FWHMs. The rms noise level measured on the difference map smoothed to the 5″ resolution is 0.025 mJy beam^{-1} at $\theta < 45''$. The SZE decrement is detected at more than 11σ statistical significance. The SZE peak is located at $3.''6$ south from the central AGN (source C1), with the SZE intensities at the two positions of -0.294 ± 0.025 mJy beam^{-1} (SZE peak) and -0.280 ± 0.025 mJy beam^{-1} (source C1 location), respectively, on the smoothed image. The offset is hence not statistically significant given the noise level of the ALMA data. The integrated SZE flux density within $\theta = 40''$ is -11.9 ± 0.4 mJy. The mean signal within the annulus at $40'' < \theta < 45''$ is consistent with zero and -0.13 ± 0.17 μJy arcsec^{-2}.

In figure 4 we plot azimuthally averaged intensity profiles in four quadrants with position angles of 315°–45° (north), 45°–135° (east), 135°–225° (south), and 225°–315° (west). The statistical error in each bin is computed using equation (1) of Kitayama et al. (2016). The SZE intensities in four quadrants are consistent with one another within the error, while the signal in the north quadrant tends to be weaker than the other directions at $\theta < 15''$.

[1] The algorithm of Multi-Scale CLEAN has been modified since CASA version 5.6.0 (Steeb & Rau 2019). We checked that the results of the present paper remain essentially unchanged by this modification as long as the Gaussian components are chosen to give maximal recovered flux and minimal residuals as described in the text.

Downloaded from https://academic.oup.com/pasj/article/72/2/33/5803376 by University of Tsukuba user on 07 October 2021

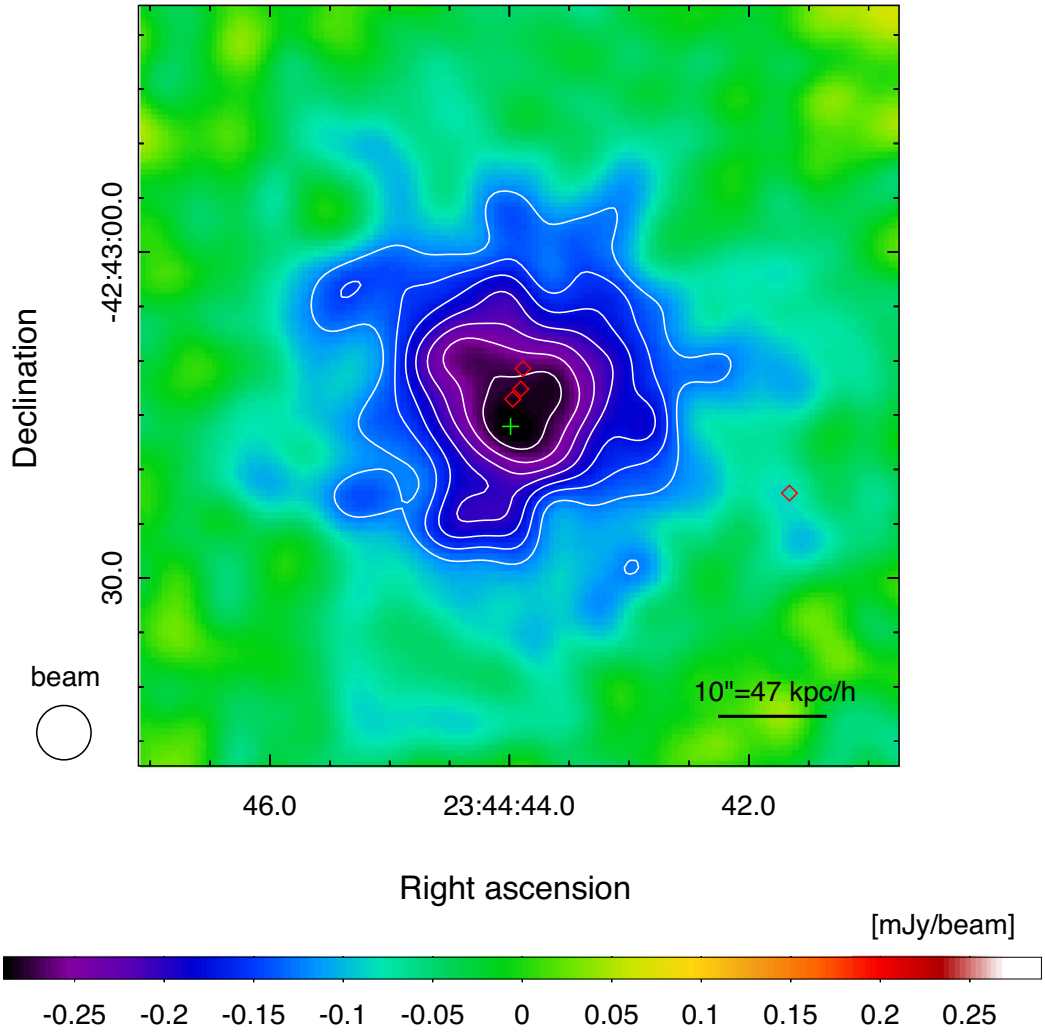

Fig. 3. ALMA SZE image of the Phoenix cluster at the central frequency of 92 GHz smoothed to have a beam size of 5″ FWHM. Contours show the statistical significance of 5–11σ in increments of $1\sigma = 0.025$ mJy beam^{-1}. The positions of the SZE peak and subtracted sources are denoted by a cross and diamonds, respectively. (Color online)

4 Interpretation and implications

4.1 Comparison to X-ray data

To compare with the ALMA SZE data, we extracted the X-ray data of the Phoenix cluster taken by Chandra ACIS-I (ObsID: 13401, 16135, 16545, 19581, 19582, 19583, 20630, 20631, 20634, 20635, 20636, and 20797). The total exposure time is 551.5 ks. The data were processed using CIAO version 4.11 (Fruscione et al. 2006) and the Calibration database (CALDB) version 4.8.2. The backgrounds were estimated from the off-center region at $3' < r < 5'$ from the central AGN, where the ICM emission is negligible. We used the data at observed energies $E = 0.7$–7.0 keV to minimize the effects of the ACIS contamination layer and the instrumental background (e.g., Bartalucci et al. 2014; Plucinsky et al. 2018). Throughout the analysis, we assumed that the ICM is in collisional ionization equilibrium, the abundance ratio of elements heavier than helium is that of Anders and Grevesse (1989), and the Galactic hydrogen column density toward the Phoenix cluster is 1.52×10^{20} cm^{-2} (Kalberla et al. 2005). We fixed the helium mass fraction at $Y = 0.25$, which is nearly unchanged between the primordial gas and the solar photosphere (e.g., Asplund et al. 2009; Planck Collaboration 2018). Spectral fitting was done with XSPEC version 12.10.0e (Arnaud 1996).

There is an X-ray bright type II quasar near the center of the Phoenix cluster (Ueda et al. 2013; McDonald et al. 2015, 2019). The 2.0–7.0 keV brightness has a prominent point-like peak at ($23^{\rm h}44^{\rm m}43\overset{\rm s}{.}962$, $-42^\circ43'12\overset{''}{.}412$) and we refer to this position as "the X-ray center" of this cluster; it agrees with the position of the central AGN (source C1) in the ALMA 92 GHz map within $0\overset{''}{.}6$. For definiteness, we denote the projected distance from the X-ray center by $\theta_{\rm X}$.

Downloaded from https://academic.oup.com/pasj/article/72/2/33/5803376 by University of Tsukuba user on 07 October 2021

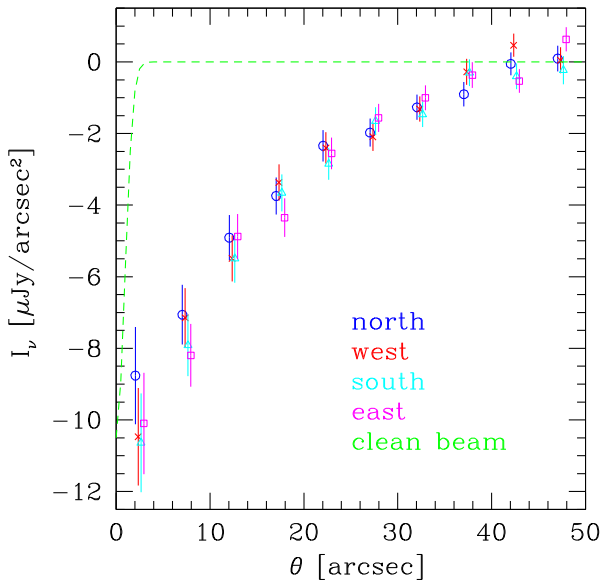

Fig. 4. Azimuthally averaged SZE intensity profiles as a function of the projected distance from the central AGN in the four quadrants; north (circles), west (crosses), south (triangles), and east (squares). For clarity, symbols are slightly shifted horizontally. The dashed line shows an azimuthally averaged shape of the synthesized beam. (Color online)

The emission around the X-ray center is dominated by the quasar and the ICM at $E > 2$ keV and $E < 2$ keV, respectively (figure 5). We modeled the spectrum of the former by an obscured (by a torus) power-law plus an iron fluorescent line at the rest-frame energy of 6.4 keV as in Ueda et al. (2013). Following McDonald et al. (2019), we also took into account additional photoelectric absorption by cool gas within the Phoenix cluster (see the next paragraph for details). Unless otherwise stated, there were in total five position-dependent free parameters in our spectral model; projected temperature of the ICM, projected metallicity of the ICM, column density of an intrinsic absorber within the cluster, and spectral normalization factors for the ICM and for the central AGN. In addition, three parameters of the central AGN (the spectral index, column density of an obscuring torus, and the flux ratio between the 6.4 keV line and the power-law continuum) were varied when fitting the spectrum at $\theta_X < 1''.5$ and fixed at their best-fitting values elsewhere.

Figure 5 explicitly shows the impact of intrinsic absorption within the Phoenix cluster mentioned above. If intrinsic absorption is not taken into account, the projected ICM temperature at $\theta_X < 1''.5$ is $kT = 9.8 \pm 1.5$ keV with $\chi^2/\mathrm{dof} = 472/401$ (left-hand panel), where dof denotes a degree of freedom of the fit. Inclusion of intrinsic absorption significantly decreases the temperature to $kT = 2.7^{+0.4}_{-0.3}$ keV and improves the fit to $\chi^2/\mathrm{dof} = 443/400$ (right-hand panel); the best-fitting hydrogen column density of the absorber $N_{\mathrm{H,int}} = (6.7 \pm 1.1) \times 10^{21}$ cm^{-2} is also consistent with figure 6 of McDonald et al. (2019). In other words, intrinsic absorption largely modifies the spectral shape at 0.7–2.0 keV and leads to a reduction of the best-fitting temperature by more than a factor of 3. This reflects the fact that the ICM continuum is overwhelmed by the AGN at $E > 2$ keV and the ICM metal lines are sensitive to intrinsic absorption at $E < 2$ keV. It is hence meaningful to perform an independent measurement of the ICM temperature without relying on the X-ray spectrum. We will discuss such a complementary probe using the SZE data in subsection 4.4.

As in Kitayama et al. (2016), we performed X-ray thermodynamic mapping using the contour binning algorithm (Sanders 2006). In addition to the central region at $\theta_X < 1''.5$ mentioned above, we defined subregions with nearly equal photon counts by adopting a signal-to-noise

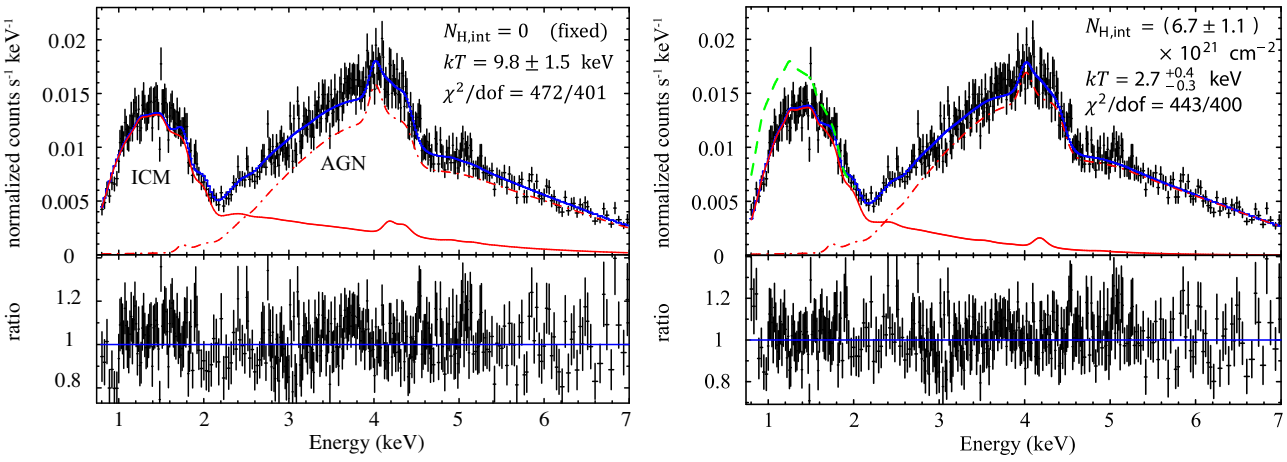

Fig. 5. Chandra X-ray spectra of the Phoenix cluster at $\theta_X < 1''.5$ (top) and the residuals with respect to the best-fitting models (bottom). Left: Lines show the best-fitting models of the ICM without intrinsic absorption (red solid), the central AGN (red dot–dashed), and their sum (blue solid). Right: Same as the left-hand panel except that intrinsic absorption within the cluster is included in the fit. For reference, a green dashed line shows the ICM spectrum at $E < 2$ keV free from intrinsic absorption. (Color online)

Downloaded from https://academic.oup.com/pasj/article/72/2/33/5803376 by University of Tsukuba user on 07 October 2021

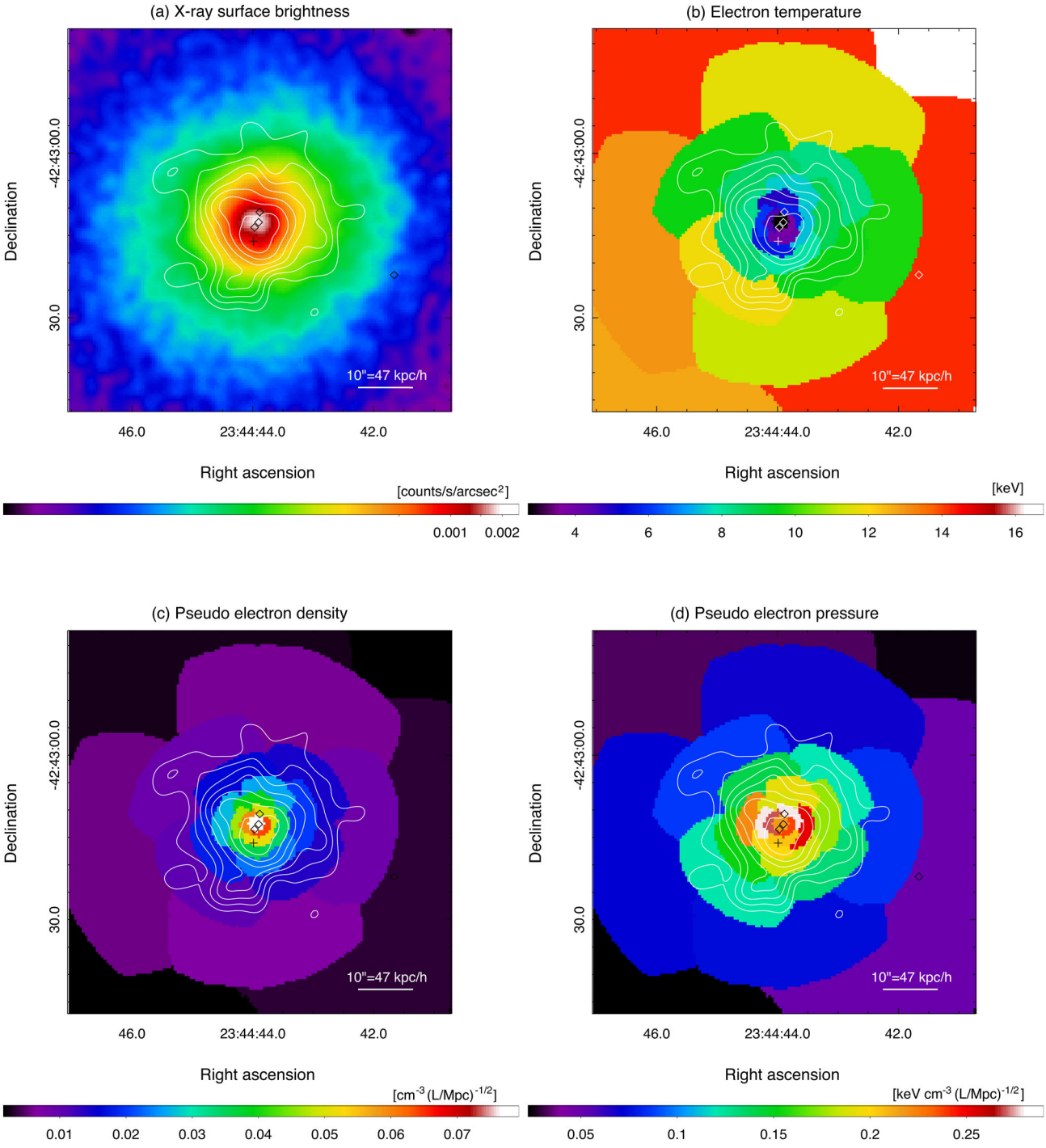

Fig. 6. Chandra X-ray maps of the Phoenix cluster. Contours show the significance levels of the ALMA SZE image plotted in figure 3, and a cross and diamonds indicate the positions of the SZE peak and subtracted sources, respectively. Subregions in panels (b), (c), and (d) are defined by the contour binning algorithm (Sanders 2006). (a) X-ray surface brightness in the 0.7–2.0 keV band in count s^{-1} $arcsec^{-2}$, smoothed by a Gaussian kernel with 2″3 FWHM. The color is shown in a logarithmic scale. (b) Projected X-ray spectroscopic temperature in keV. (c) Pseudo-electron density in $cm^{-3} \times (L/\mathrm{Mpc})^{-1/2}$ assuming a uniform line-of-sight depth of L. (d) Pseudo-electron pressure in keV $cm^{-3} \times (L/\mathrm{Mpc})^{-1/2}$. (Color online)

ratio (S/N) threshold of 100 (i.e., ∼10000 counts) in the 0.7–7.0 keV band. The 0.7–7.0 keV spectrum in each subregion was fitted by the model mentioned above. Typical statistical errors are 25% and 5% for the temperature and the density of the ICM, respectively; the errors are mainly driven by the limited energy range, particularly near the central AGN, available for determining the ICM properties. We also checked that the AGN emission is consistent with the point spread function (PSF) of ACIS-I and becomes negligible at $\theta_X > 5''$; we excluded the AGN emission

Downloaded from https://academic.oup.com/pasj/article/72/2/33/5803376 by University of Tsukuba user on 07 October 2021

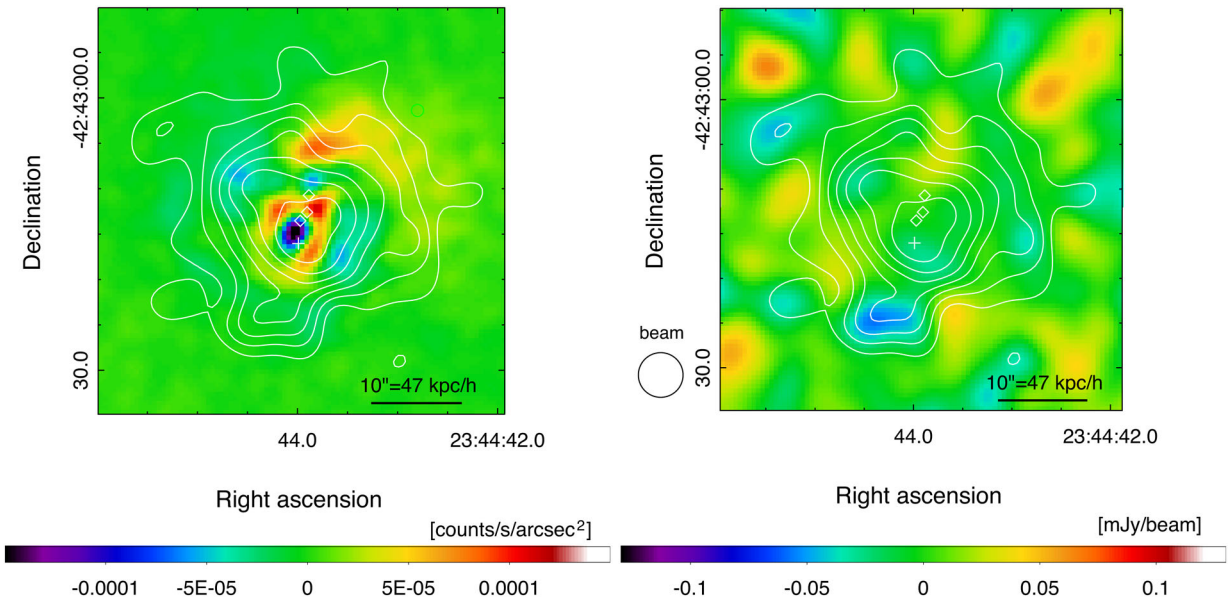

Fig. 7. Residual X-ray and SZE images of the Phoenix cluster after subtracting the mean signal as described in the text. Left: Chandra X-ray surface brightness in the 0.7–2 keV band, smoothed by a Gaussian kernel with 2.″3 FWHM. Right: ALMA SZE brightness at 92 GHz smoothed to 5″ FWHM with the rms noise of 0.025 mJy beam^{-1}. In both panels, contours show the significance levels of the ALMA SZE image plotted in figure 3, and a cross and diamonds indicate the positions of the SZE peak and subtracted sources, respectively. (Color online)

in the spectral fitting at such distances. The absorption-corrected intrinsic AGN luminosity is $L_{\rm X}(0.7\text{–}7.0\ {\rm keV}) = (1.81 \pm 0.09) \times 10^{45}\, h^{-2}\ {\rm erg\ s^{-1}}$, which amounts to ∼40% of the X-ray luminosity from the entire ICM.

Figure 6 shows X-ray measured quantities overlaid with the ALMA SZE contours. The 0.7–2.0 keV surface brightness [panel (a)] traces the line-of-sight integral of density squared of the ICM, which is highly concentrated around the central AGN. On the other hand, projected temperature [panel (b)] drops to ∼3 keV near the center and is lower in the north–south direction. Pseudo electron density, assuming a uniform line-of-sight depth of L [panel (c)], tends to be higher in the north–south direction across the center. Consequently, pseudo electron pressure [panel (d)], a product of the quantities plotted in panels (b) and (c), is less concentrated than the density; it decreases only by a factor of ∼2 from the center to $\theta \sim 15''$. Note that absolute values of the pseudo pressure are arbitrary ($\propto L^{-1/2}$) and the plotted values are also subject to statistical errors of ∼25%. The overall trend of the pseudo pressure map still shows qualitative agreement with the ALMA SZE image.

To further examine the departure from symmetry in the observed X-ray and SZE data, in figure 7 we plot residual images after subtracting the mean signal in a model-independent manner. For this purpose, we first searched for an ellipse that minimizes the variance of the 0.7–2.0 keV X-ray brightness relative to its mean at $\bar{\theta}_{\rm X} < 5''$, where $\bar{\theta}_{\rm X}$ is the geometrical mean of semi-major and semi-minor axis lengths around the X-ray center. We found that such an ellipse has the axis ratio of 0.97, a position angle of −112°, and its center at (ΔRA, ΔDec) = (0.″1, −0.″2) from the X-ray center. We then computed the mean X-ray brightness over this ellipse as a function of $\bar{\theta}_{\rm X}$ and subtracted it from the X-ray brightness at each sky position. We also subtracted from the SZE image the mean SZE brightness over the same ellipse as used for the X-ray image.

Figure 7 confirms the presence of X-ray cavities and overdense regions around the central AGN reported previously (McDonald et al. 2015, 2019). It further shows the absence of significant disturbance in the residual SZE image above the noise level ($1\sigma = 0.025$ mJy beam^{-1} at 5″ FWHM). This suggests that the ICM in this region is consistent with being isobaric.

To be more quantitative, we applied the same method as in subsection 3.4 of Ueda et al. (2018) and inferred the equation of state of observed perturbations. Within 10″ from the X-ray center and assuming the line-of-sight depth of $l = 100$ kpc, the X-ray data give $|\Delta I_{\rm X}|/\langle I_{\rm X}\rangle = 0.115$, $kT = 5.9 \pm 0.3$ keV, and $\sqrt{\langle n_{\rm e}^2\rangle} = (0.102 \pm 0.001)(l/100\ {\rm kpc})^{-1/2}\ {\rm cm^{-3}}$, where $I_{\rm X}$ is the X-ray surface brightness and $n_{\rm e}$ is the electron number density. Using equation (4) of Ueda et al. (2018), we obtained the mass density perturbation of $\Delta\rho = (1.14 \pm 0.02) \times 10^{-26}(l/100\ {\rm kpc})^{-1/2}\ {\rm g\ cm^{-3}}$. For the same region, the SZE data give 1σ upper limit on the pressure perturbation of $\Delta p < 1.17 \times 10^{-10}(l/100\ {\rm kpc})^{-1}\ {\rm erg\ cm^{-3}}$. They lead to an upper limit on $w \equiv \Delta p/\Delta\rho$ of $\sqrt{w} < 1010(l/100\ {\rm kpc})^{-1/4}\ {\rm km\ s^{-1}}$. While the limit is still weak,

Downloaded from https://academic.oup.com/pasj/article/72/2/33/5803376 by University of Tsukuba user on 07 October 2021

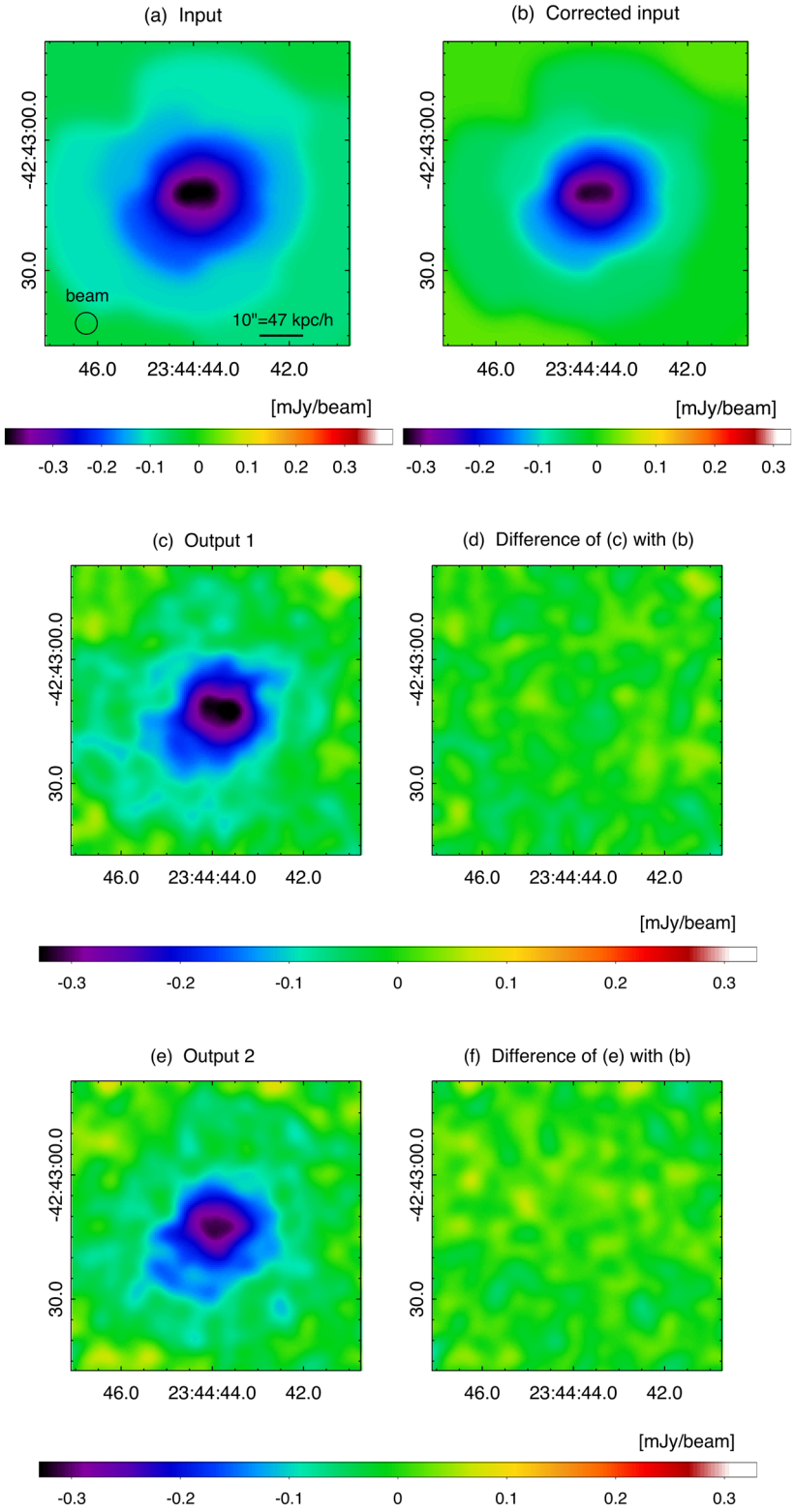

Fig. 8. Mock SZE images of the Phoenix cluster at 92 GHz with $y_{\rm peak} = 8 \times 10^{-4}$. All the images have been smoothed to 5″ FWHM. (a) Input model. (b) Input model to which the correction by equation (1) has been applied. (c) Simulation output including noise. (d) Difference of panel (c) with panel (b). (e) Same as panel (c) but with different noise realization. (f) Difference of panel (e) with panel (b). Note that the range of the color scale is wider in panel (a) than in the other panels. (Color online)

Downloaded from https://academic.oup.com/pasj/article/72/2/33/5803376 by University of Tsukuba user on 07 October 2021

the observed perturbations in the Phoenix cluster core is consistent with being isobaric, i.e., $\sqrt{w} < c_s$, where $c_s = 1250(kT/5.9\ \mathrm{keV})^{1/2}\ \mathrm{km\ s^{-1}}$ is the adiabatic sound speed.

4.2 Imaging simulations

To understand the degree of the missing flux of the ALMA SZE data, we performed imaging simulations using the X-ray pseudo pressure map (figure 6d) of the Phoenix cluster. Given that absolute values of the pseudo pressure were arbitrary, they were normalized so that the peak signal corresponds to the Compton y-parameter of $y_{\mathrm{peak}} = 8 \times 10^{-4}$, which is a typical value for massive cool core clusters. To take into account uncertainties of this normalization, we also examined the cases of $y_{\mathrm{peak}} = 4 \times 10^{-4}$ and 12×10^{-4}. A relativistic correction to the SZE intensity by Itoh and Nozawa (2004) was applied adopting the projected temperature shown in figure 6b at each sky position.

We created model images separately at four spectral windows centered at 85, 87, 97, and 99 GHz with an effective bandwidth of 1.875 GHz each. The pointing directions, the array configuration, the hour angle, the total effective integration time, and the average precipitable water vapor were set to match those of each executing block of real observations. Visibility data were then produced using the CASA task *simobserve* including both instrumental and atmospheric thermal noise in each spectral window. The rms levels of dirty images are consistent with the values given in table 1. The mock visibility was deconvolved in the same way as the real data as described in subsection 3.2. For each value of y_{peak}, we repeated the above procedure 10 times, adopting different noise realizations. To correct for any potential bias in producing an image at a single frequency from the data taken over finite bandwidths, the simulation results are compared with an input model evaluated at the central frequency 92 GHz.

Figure 8 compares two arbitrarily chosen realizations of the simulated images and the input model. The azimuthal average of all realizations of simulated images are plotted in figure 9. The simulated images for $y_{\mathrm{peak}} = 8 \times 10^{-4}$ show similar amplitude and spatial extension to the real data plotted in figures 3 and 4. Figures 8 and 9 also illustrate that the simulated images are in good agreement with the input model once the correction by equation (1) described below is applied. The rms values at $\theta < 45''$ in figures 8d and 8f are both 0.022 mJy beam^{-1} and fully consistent with noise.

As in Kitayama et al. (2016), we find that the simulation results on average follow the linear relation

$$I_\nu^{\mathrm{out}} = c_1 I_\nu^{\mathrm{in}} + c_0, \quad (1)$$

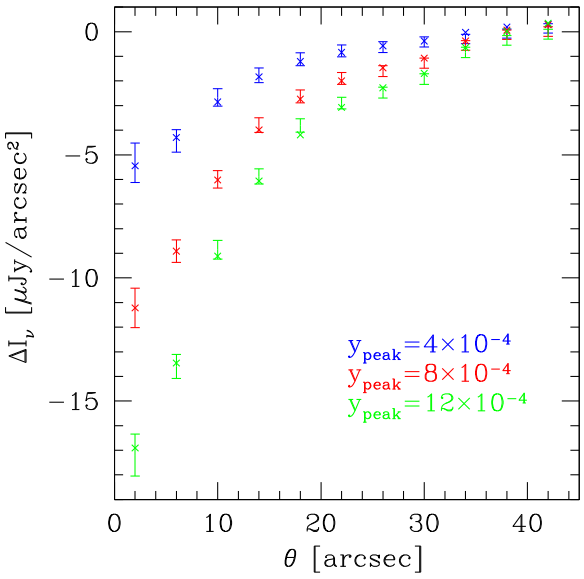

Fig. 9. Error bars show azimuthally averaged intensity profile of the simulation outputs at 92 GHz with $y_{\mathrm{peak}} = 4 \times 10^{-4}$ (blue), 8×10^{-4} (red), and 12×10^{-4} (green). For each value of y_{peak}, the results of 10 realizations are averaged. Crosses show the same quantity from the input model to which the correction by equation (1) has been applied for each value of y_{peak}. (Color online)

where I_ν^{out} and I_ν^{in} are, respectively, the intensities of output and input images at the same sky position. Figure 10 shows that the coefficient c_0 is sensitive to the adopted value of y_{peak} whereas c_1 remains nearly unchanged and is close to unity. We hence determined c_0 and c_1 by fitting the results of 10 simulation realizations for each value of y_{peak}, where c_1 is assumed to be common among different values of y_{peak}. This yielded $c_1 = 0.94 \pm 0.02$ and $c_0 = (1.19 \pm 0.16,\ 2.07 \pm 0.20,\ 3.02 \pm 0.28)\ \mu\mathrm{Jy\ arcsec^{-2}}$ for $y_{\mathrm{peak}} = (4 \times 10^{-4}, 8 \times 10^{-4}, 12 \times 10^{-4})$, respectively. The error bars of I_ν^{out} plotted in figure 10 show the standard deviation in each bin and are dominated by statistical errors; each bin contains on average 8000 pixel data (i.e., 800 per realization). The rms deviation of the mean values of $(I_\nu^{\mathrm{out}}, I_\nu^{\mathrm{in}})$ from the best-fitting relation is $\Delta I_\nu^{\mathrm{in}} = 0.17 \mu\mathrm{Jy\ arcsec^{-2}}$ and gives an estimate of intrinsic deviation from equation (1) apart from the statistical errors. We regard $\sqrt{2}$ times this value (i.e., $\Delta I_\nu^{\mathrm{in}} = 0.24\ \mu\mathrm{Jy\ arcsec^{-2}}$) as the 1σ systematic uncertainty in the true intensity when a constant offset (corresponding to c_0) is subtracted. In real observations, the true intensity is unknown and we will subtract the mean signal at the edge of the emission profile instead of assuming any specific value of c_0 in subsections 4.3 and 4.4.

The fact that the simulated images of the Phoenix cluster are well reproduced by equation (1) with the value of c_1 close to unity (figures 8–10) confirms that the observed ALMA SZE image gives a reasonable representation of differential values of the true intensity (Kitayama et al. 2016).

Downloaded from https://academic.oup.com/pasj/article/72/2/33/5803376 by University of Tsukuba user on 07 October 2021

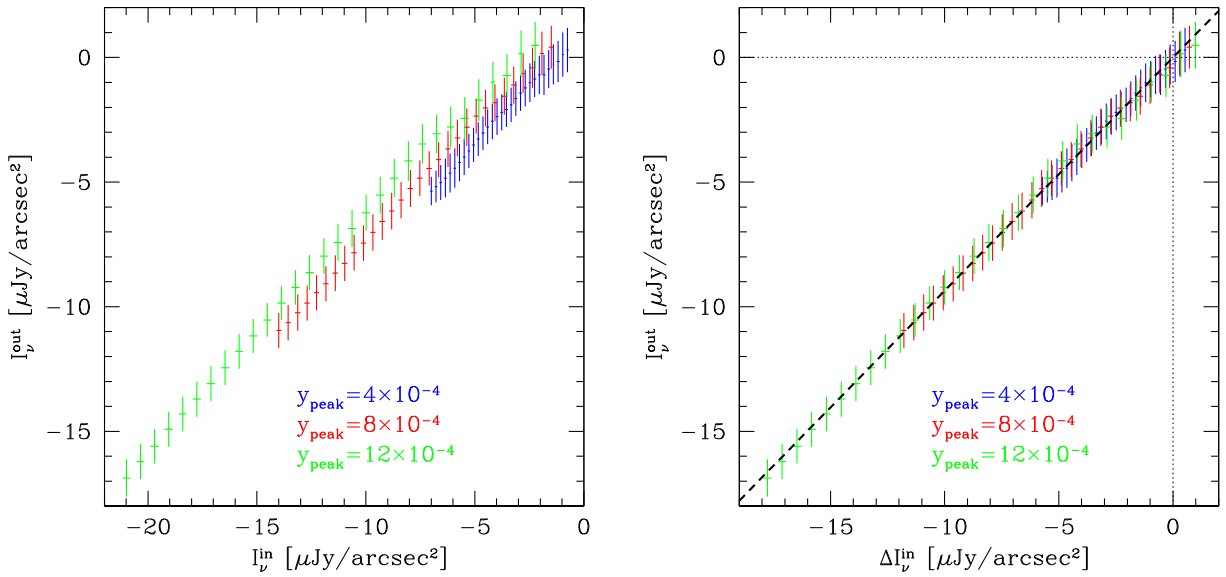

Fig. 10. Left: Relation between the output intensity and the input intensity at 92 GHz from the imaging simulations with $y_{\rm peak} = 4 \times 10^{-4}$ (blue), 8×10^{-4} (red), and 12×10^{-4} (green). Error bars denote the standard deviation in each bin. Right: Same as the left-hand panel, except that the fitted value of c_0/c_1 in equation (1) has been added to $I_\nu^{\rm in}$ to give zero intercept in each case. The thick dashed line shows the best-fitting relation with $c_1 = 0.94$. (Color online)

Figure 9 further implies that the extended signal is retained out to $\theta \sim 40''$ irrespectively of the adopted value of $y_{\rm peak}$, i.e., normalization of the intrinsic signal.

4.3 Compton *y*-parameter map and the inner pressure profile

A high angular resolution SZE image provides a direct probe of the projected electron pressure, or equivalently, the Compton y-parameter, of the ICM. Figure 11 shows the Compton y-parameter map reconstructed from the observed ALMA image in figure 3 using the results of subsection 4.2. Specifically, the ALMA image was divided by the correction factor for the missing flux of 0.94 [c_1 in equation (1)] and the mean signal (consistent with zero) at $\theta = 42''$ was subtracted. At each sky position, the relativistic correction by Itoh and Nozawa (2004) was applied adopting the projected X-ray spectroscopic temperature shown in figure 6b. The plotted values correspond to the incremental y-parameter (Δy) relative to the sky positions at $\theta = 42''$. The peak value is $\Delta y = (5.3 \pm 0.4[\text{statistical}] \pm 0.3[\text{systematic}]) \times 10^{-4}$, where the systematic error is from the absolute calibration of ALMA (6%: Kitayama et al. 2016) and the missing flux correction (0.24 μJy arcsec^{-2}: subsection 4.2). Within the inferred range of statistical and systematic uncertainties, the overall morphology of the Compton y-parameter map does not exhibit deviation from that of X-rays.

Given the regularity of the Compton y-parameter map, we compare its azimuthal average to the mean radial pressure profiles of various galaxy cluster samples in figure 12. Vertical error bars include both statistical and systematic errors, whereas horizontal ones indicate the bin size; the bins are geometrically spaced with the inner-most bin at $0 < \theta < 4''$ and the size increasing by a factor of 1.1 so that the statistical error is smaller than 15% in each bin. The mean radial pressure profiles are computed by integrating the generalized NFW profile (Nagai et al. 2007) along the line-of-sight with the model parameters given in the literature (mentioned below) assuming $M_{500} = 8.8 \times 10^{14}\, h^{-1}\, M_\odot$ and $r_{500} = 0.92\, h^{-1}$ Mpc at $z = 0.597$ for the Phoenix cluster (McDonald et al. 2012),[2] being convolved with the synthesized beam size of ALMA ($2''.25 \times 1''.92$ FWHMs), and taking a difference with respect to the positions at $42''$ from the center. We find that the inner pressure profile of the Phoenix cluster is in good agreement with the expectation from the local cool core clusters by Arnaud et al. (2010) and is clearly steeper than that from more distant counterparts by Planck Collaboration (2013) and McDonald et al. (2014b). McDonald et al. (2015) showed that the Chandra X-ray data of this cluster also agree with the pressure profile of the local cool core clusters of Arnaud et al. (2010). These results further imply that azimuthally averaged SZE and X-ray data of the Phoenix cluster are consistent with each other.

[2] M_{500} is the total mass enclosed within the radius r_{500} at which the enclosed overdensity is 500 times the critical density of the Universe at that redshift.

Downloaded from https://academic.oup.com/pasj/article/72/2/33/5803376 by University of Tsukuba user on 07 October 2021

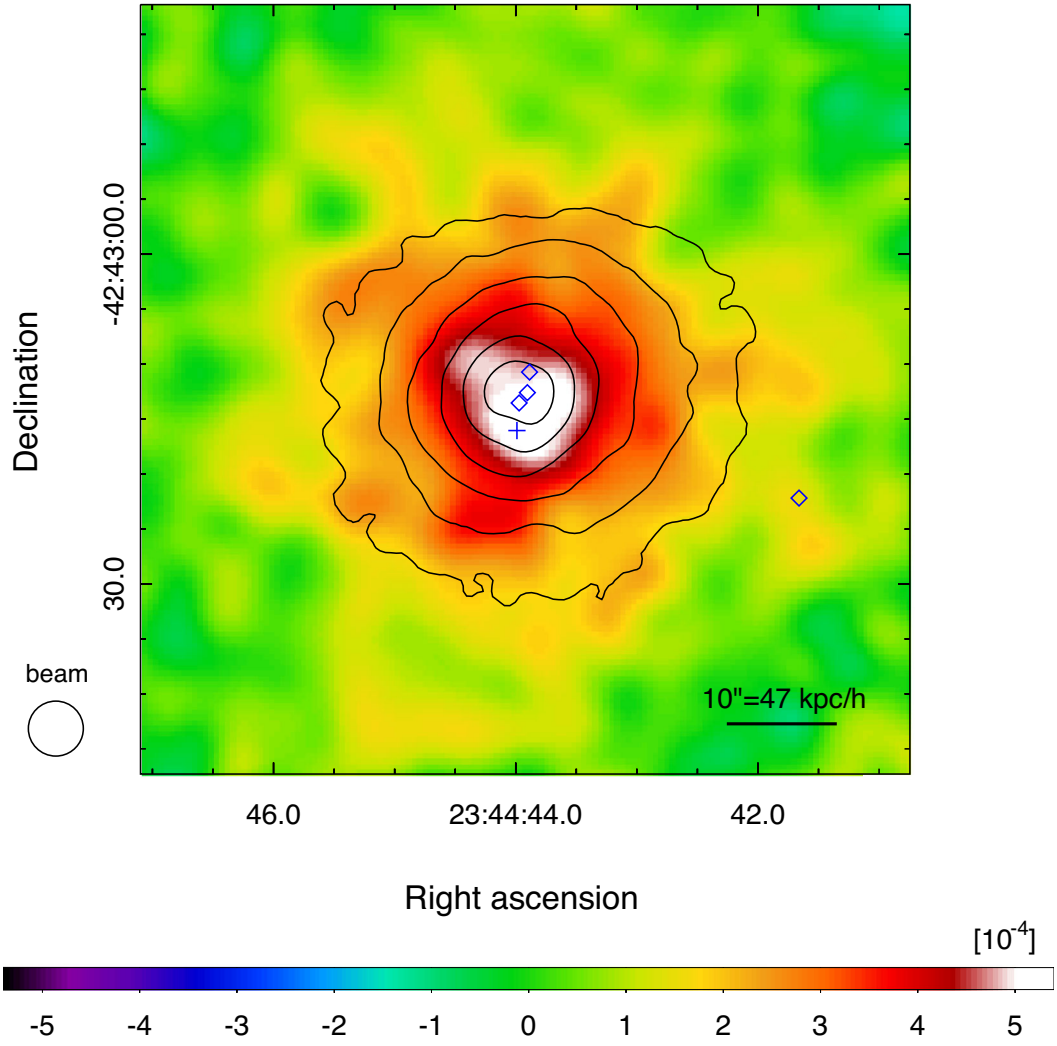

Fig. 11. Compton y-parameter map of the Phoenix cluster at 5″ resolution. The map is corrected for the missing flux and the zero level is taken at 42″ from the central AGN. Overlaid are the contours of the X-ray surface brightness at 0.7–2.0 keV by Chandra corresponding to 64%, 32%, 16%, 8%, 4%, and 2% of the peak value, after being smoothed by a Gaussian kernel with 2.″3 FWHM. The positions of the SZE peak and subtracted sources are marked by a cross and diamonds, respectively. (Color online)

4.4 Deprojected electron temperature and density

A combination of SZE and X-ray images provides a measure of temperature and density of the ICM independently of the X-ray spectroscopy (e.g., Kitayama et al. 2004; Nord et al. 2009; Basu et al. 2010). Assuming spherical symmetry and $h = 0.7$ for this particular purpose, we performed non-parametric deprojection of electron density n_e and temperature T as described in detail below. A major advantage of this method is that the impact of X-ray absorbing gas described in subsection 4.1 is minimized. If the absorbed and unabsorbed X-ray brightness is related by $I_X^{abs} = \alpha I_X^{unabs}$ $(0 \leq \alpha \leq 1)$, deprojected density and temperature vary approximately as $n_e^{abs} = n_e^{unabs}/\sqrt{\alpha}$ and $T^{abs} = T^{unabs}\sqrt{\alpha}$, respectively. The intrinsic absorption inferred in subsection 4.1 gives $\alpha \sim 0.75$ at $\theta < 1.''5$ in the 0.7–2.0 keV band, implying that the central density and temperature are expected to change only by ∼13%.

We first took geometrically-spaced bins on the sky with the inner-most bin at $0 < \theta < 4''$ (corresponding to the deprojected spherical shell of $0 < r < 26.7$ kpc) and the size increasing by a factor of 1.3 so that a statistical error is smaller than 10% in each bin. Systematic errors from the flux calibration of ALMA (6%), the missing flux correction of the SZE ($0.24\,\mu$Jy arcsec^{-2}), and the effective area of Chandra ACIS-I (4%) were added in quadrature to the statistical error in each bin. We then fitted the volume-averaged brightness in each bin of the SZE at $\theta < 40''$ and of the 0.7–2.0 keV X-rays at $\theta < 100''$ together, varying the deprojected temperature and density in each spherical shell. As the temperature at $r > 250$ kpc ($\theta > 37''$) cannot be constrained by the ALMA data, it was fixed at the

Downloaded from https://academic.oup.com/pasj/article/72/2/33/5803376 by University of Tsukuba user on 07 October 2021

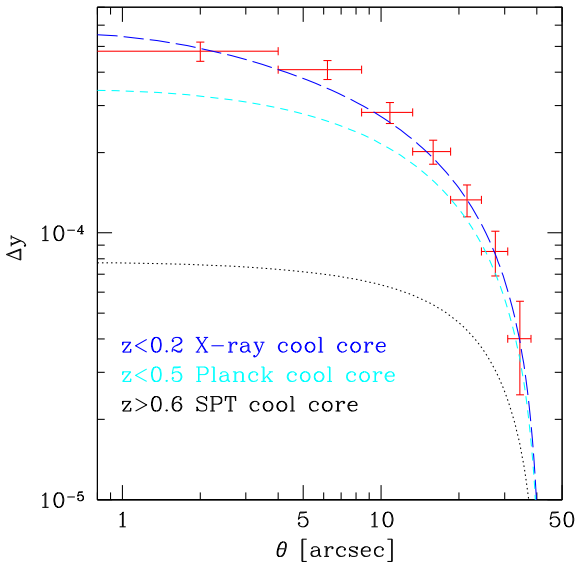

Fig. 12. Azimuthally averaged Compton y-parameter of the Phoenix cluster. Overlaid are the expectations from the generalized NFW pressure profile of X-ray selected cool core clusters at $z < 0.2$ (long dashed line) by Arnaud et al. (2010), Planck-selected cool core clusters at $z < 0.5$ (short dashed line) by Planck Collaboration (2013), and SPT-selected cool core clusters at $z > 0.6$ (dotted line) by McDonald et al. (2014b). Both the data points and the expectations are relative to the positions at $\theta = 42''$. (Color online)

projected mean value of 15.8 keV by the X-ray spectral analysis described in subsection 4.1; we checked that the deprojected quantities at $r < 100$ kpc are essentially unchanged by this assumption. For the SZE, we modeled and fitted the incremental brightness relative to the bin centered at $\theta = 43\farcs6$; the missing flux correction factor of 0.94 and the temperature-dependent relativistic correction were applied to the model brightness in each spherical shell. The X-ray emissivity was computed by SPEX v3.0.5.00 (Kaastra et al. 1996), fixing the metal abundance at 0.35 times the solar value. To examine the impact of intrinsic absorption within the Phoenix cluster, the hydrogen column density in the inner-most bin was assumed to be either $N_{\rm H,int} = 6.7 \times 10^{21}$ cm^{-2} or $N_{\rm H,int} = 0$; the former value was chosen as a limiting case of strong absorption throughout the inner 27 kpc. Note that the X-ray emission from the central AGN is negligible in the 0.7–2.0 keV band used in the analysis.

For comparison, we separately performed a deprojection analysis using solely the X-ray data. The 0.7–7.0 keV X-ray spectra in six circular annuli at $\theta = 0''$–$3''$, $3''$–$6''$, $6''$–$12''$, $12''$–$24''$, $24''$–$48''$, and $48''$–$96''$ were fitted together using the model *projct* implemented in XSPEC version 12.10.0e (Arnaud 1996). For simplicity, only statistical errors were taken into account in this particular analysis. The position-dependent free parameters were the same as those described in subsection 4.1 except that they were assigned to each of six spherical shells corresponding to the above-mentioned annuli. The spectral index, column density of an obscuring torus, and the flux ratio between the 6.4 keV line and the power-law continuum of the central AGN were fixed at their best-fitting values obtained in subsection 4.1.

Figure 13 shows deprojected temperatures obtained by two different methods described above. As expected, the results from the SZE and X-ray images are insensitive to intrinsic absorption; the temperature at $r < 27$ kpc is 2.70 ± 1.71 keV and 3.01 ± 1.86 keV with and without intrinsic absorption, respectively. Those solely from the X-ray data are much more sensitive, albeit with smaller statistical errors; the temperature at $r < 20$ kpc changes by more than a factor of 2 from $2.73^{+0.24}_{-0.22}$ keV to $6.37^{+0.73}_{-0.58}$ keV once intrinsic absorption is neglected. If intrinsic absorption is taken into account, the temperature profile from the latter deprojection method comes to a good agreement with that from the former.

Also plotted for reference in figure 13 are the mean profiles of local and distant cool core clusters (Vikhlinin et al. 2006; McDonald et al. 2014b), using the average temperature within r_{500} of this cluster, $kT_{500} = 12.6$ keV, expected from the X-ray scaling relation by Reichert et al. (2011). We find that the deprojected temperatures at $r < 100$ kpc are systematically lower than the average profiles of both local and distant clusters. The inferred central temperature is $\sim$5 times lower than the mean temperature ($\sim$16 keV) at $r > 300$ kpc. This is a much larger factor of reduction than observed in other clusters and supports that radiative cooling is efficient in the Phoenix cluster.

Given that the pressure profile of the Phoenix cluster matches that of local cool core clusters well (subsection 4.3), gas density should have been enhanced to compensate for the reduced temperature. Figure 14 shows that this is indeed the case; overlaid are the best-fitting density profiles by Vikhlinin et al. (2006) of typical local cool core clusters, Abell 2029 and Abell 1795. To correct for different size and redshift of individual clusters, these profiles have been scaled so that r gives the same fraction of r_{500} as the Phoenix cluster and that the normalization of $n_{\rm e}$ evolves to $z = 0.597$ by the same fraction as the critical density of the Universe. Gas density of the Phoenix cluster is in good agreement with those of Abell 2029 and Abell 1795 at $r > 0.2\,r_{500}$ $\sim$300 kpc, whereas it is systematically higher at smaller radii. Figure 14 also confirms that density profiles obtained from two deprojection methods are consistent with each other.

Figure 15 further illustrates that the entropy $K \equiv kTn_{\rm e}^{-2/3}$ decreases to <10 keV cm^2 at $r < 27$ kpc. Also plotted are a model $K \propto r^{1.2}$, which tends to give a lower limit to non-radiative clusters at $r \lesssim 0.5\,r_{500}$ (Voit et al. 2005), and a prediction $K \propto r^{1.4}$ for the steady-state cooling flow (Voit 2011); both profiles are normalized to match the

Downloaded from https://academic.oup.com/pasj/article/72/2/33/5803376 by University of Tsukuba user on 07 October 2021

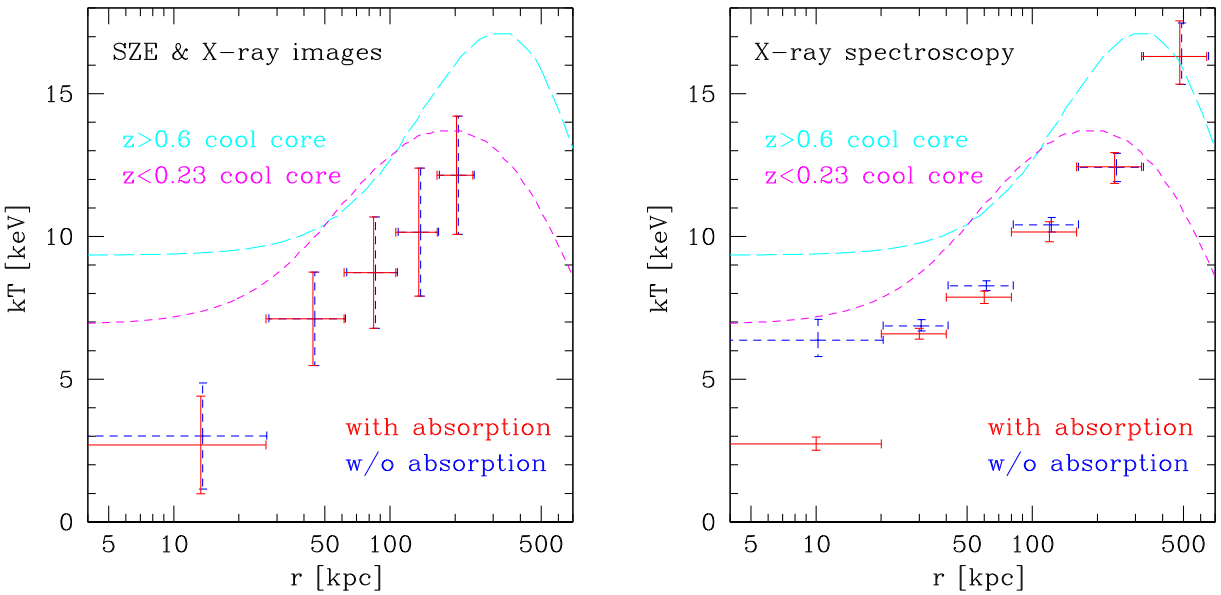

Fig. 13. Deprojected temperature profiles of the Phoenix cluster from SZE and X-ray images (left-hand panel) and from X-ray spectroscopy (right-hand panel) assuming $h = 0.7$. The error bars show the results with (solid) or without (dashed) intrinsic absorption inside the cluster. For clarity, dashed error bars are slightly shifted horizontally. Lines indicate the mean profiles of cool core clusters at $z > 0.6$ (long-dashed) by McDonald et al. (2014b) and at $z < 0.23$ (short-dashed) by Vikhlinin et al. (2006). (Color online)

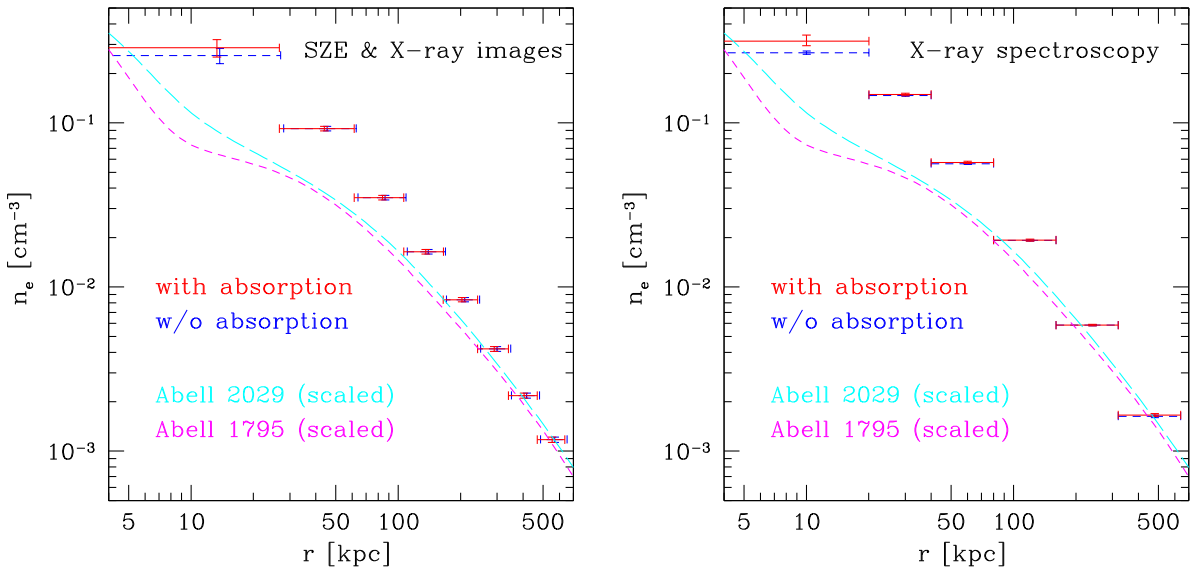

Fig. 14. Same as figure 13, except showing deprojected electron density. Lines indicate the profiles of local cool core clusters Abell 2029 (long-dashed) and Abell 1795 (short-dashed) by Vikhlinin et al. (2006); both profiles are scaled to match the radius and redshift of the Phoenix cluster as described in the text. In the left-hand panel, the data points at $r > 250$ kpc are obtained solely from the X-ray image assuming $kT = 15.8$ keV. (Color online)

data point in the outer-most bin in the left-hand panel. The observed entropy profile shows a better agreement with $K \propto r^{1.4}$ than $K \propto r^{1.2}$ and strongly supports that radiative cooling is efficient in the Phoenix cluster.

Finally, we plot in figure 16 the radiative cooling time, i.e., total thermal energy of the gas divided by the bolometric luminosity in each radial bin. As the bolometric luminosity of the gas at $kT \gtrsim 1$ keV is dominated by X-rays, it is computed by integrating the rest-frame X-ray emissivity provided by SPEX over photon energies (e.g., Schure et al. 2009). The radial profile of the cooling time is well represented by a single power-law of $t_{\rm cool} \propto r^{1.7}$ and drops to $\sim$0.1 Gyr at $r < 27$ kpc.

4.5 How much gas is cooling in the Phoenix cluster?

The results in subsection 4.4 immediately yield the amount of $\sim$3 keV gas within $r = 27$ kpc to be $M_{\rm cool} = (6.4 \pm 0.9) \times 10^{11}\,M_\odot$. This corresponds to $\sim$20% of the stellar mass

Downloaded from https://academic.oup.com/pasj/article/72/2/33/5803376 by University of Tsukuba user on 07 October 2021

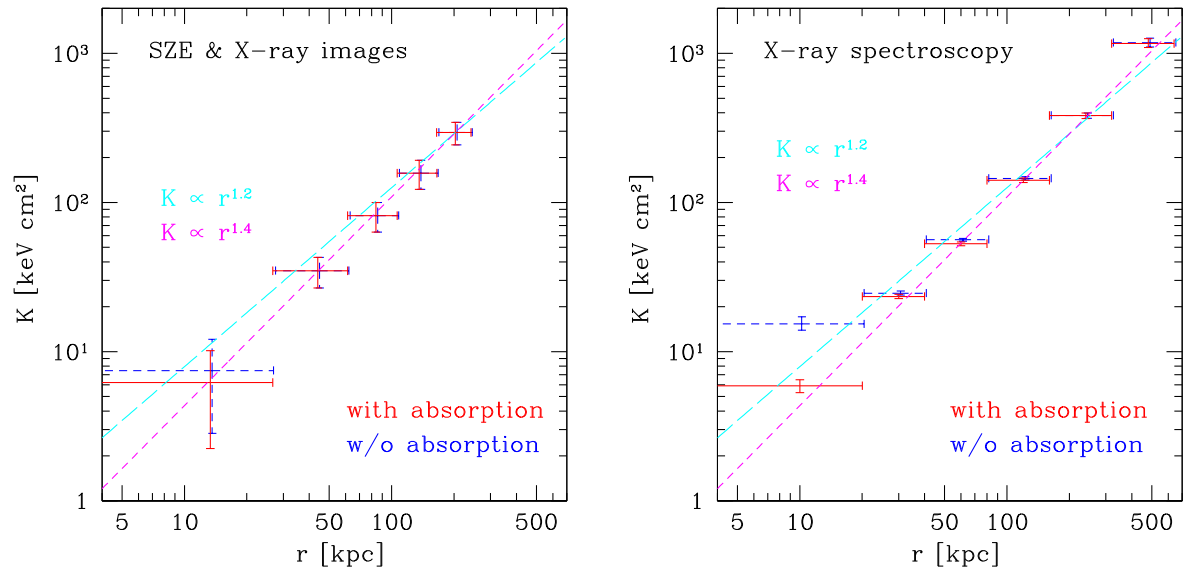

Fig. 15. Same as figure 13, except showing entropy. Lines indicate the model profiles $K \propto r^{1.2}$ (long-dashed) (Voit et al. 2005) and $K \propto r^{1.4}$ (short-dashed) (Voit 2011), both normalized to match the data point in the outer-most bin in the left-hand panel. (Color online)

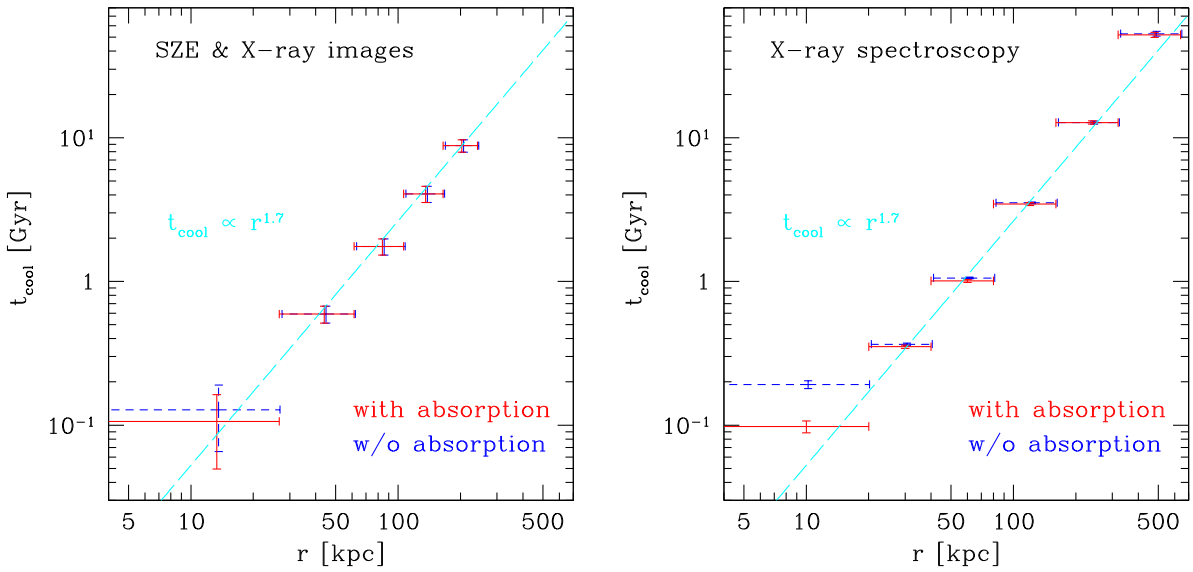

Fig. 16. Same as figure 13 except for showing the radiative cooling time. The dashed line indicates the relation $t_{\rm cool} \propto r^{1.7}$, normalized to match the data point in the outer-most bin in the left-hand panel. (Color online)

$\sim 3 \times 10^{12}\,M_\odot$ in the central galaxy of the Phoenix cluster (McDonald et al. 2012, 2013). If the mass deposition rate at $kT \gtrsim 3$ keV is $\dot{M}_{\rm cool} \sim 2000\,M_\odot\,{\rm yr}^{-1}$, as indicated by the X-ray data (e.g., McDonald et al. 2013; Ueda et al. 2013), the cool gas should have accumulated over the period

$$\tau_{\rm acc} = \frac{M_{\rm cool}}{\dot{M}_{\rm cool}} = (0.32 \pm 0.05) \left(\frac{\dot{M}_{\rm cool}}{2000\,M_\odot\,{\rm yr}^{-1}} \right)^{-1} {\rm Gyr}. \quad (2)$$

This is feasible because $t_{\rm cool} < \tau_{\rm acc}$ is achieved out to $r > 27$ kpc (figure 16). The required inflow velocity of the gas,

$$v = \frac{\dot{M}_{\rm cool}}{4\pi r^2 \rho} = 62 \left(\frac{r}{30\,{\rm kpc}} \right)^{-2} \left(\frac{n_{\rm e}}{10^{-1}\,{\rm cm}^{-3}} \right)^{-1} \times \left(\frac{\dot{M}_{\rm cool}}{2000\,M_\odot\,{\rm yr}^{-1}} \right) {\rm km\,s}^{-1}, \quad (3)$$

is also much smaller than the adiabatic sound speed $c_s \simeq 900(kT/3\,{\rm keV})^{1/2}$ km s^{-1} over the range of radii considered in this paper.

Downloaded from https://academic.oup.com/pasj/article/72/2/33/5803376 by University of Tsukuba user on 07 October 2021

Our results consistently imply that radiative cooling is hardly suppressed down to $kT \sim 3$ keV. At even lower temperatures, previous works infer that cooling may weaken moderately with the mass deposition rate of $\dot{M}_{\rm cool} = 130$–$480\ M_\odot\ {\rm yr}^{-1}$ for the gas below 2 keV (Pinto et al. 2018) and the star formation rate of $\dot{M}_{\rm SF} = 400$–$900\ M_\odot\ {\rm yr}^{-1}$ in the central galaxy (McDonald et al. 2012, 2013; Mittal et al. 2017). If this is the case, the time required for the above-mentioned cool gas to turn into stars will be

$$\tau_{\rm SF} = \frac{M_{\rm cool}}{\dot{M}_{\rm SF}} = (1.3 \pm 0.2) \left(\frac{\dot{M}_{\rm SF}}{500\ M_\odot\ {\rm yr}^{-1}} \right)^{-1} {\rm Gyr}, \qquad (4)$$

i.e., the stellar mass of the central galaxy is expected to increase by ∼20% over this period.

5 Conclusions

We have presented the SZE image of the Phoenix galaxy cluster at $z = 0.597$ taken by ALMA in Band 3. The SZE is imaged at $5''$ resolution (or $23\,h^{-1}$ kpc) within $200\,h^{-1}$ kpc from the central AGN with a peak S/N exceeding 11. Combined with the Chandra X-ray image, the ALMA SZE data further allow for non-parametric deprojection of electron temperature, density, and entropy. Our method can minimize contamination by the central AGN and the X-ray absorbing gas within the cluster, both of which largely affect the X-ray spectrum.

We find no significant asymmetry or disturbance in the SZE image within the current measurement errors. The detected signal shows much higher central concentration than other distant clusters and agrees well with the average pressure profile of local cool-core clusters. Unlike in typical clusters at any redshift, the gas temperature drops by at least a factor of 5 toward the center. In the inner $20\,h^{-1}$ kpc, we identify the presence of $\sim 6 \times 10^{11}\ M_\odot$ cool gas with $kT \sim 3$ keV, the amount of which corresponds to ∼20% of the stellar mass in the central galaxy. The low entropy (∼10 keV cm^2) and the short cooling time (∼0.1 Gyr) of this gas further corroborates that radiative cooling is hardly suppressed between $kT \sim 16$ keV and $kT \sim 3$ keV. Taken together, our results imply that the gas is cooling efficiently and nearly isobarically down to the inner $20\,h^{-1}$ kpc in the Phoenix cluster.

Acknowledgments

We thank the anonymous referee and Luca Di Mascolo for their helpful comments. This paper makes use of the following ALMA data: ADS/JAO.ALMA#2015.1.00894.S. The scientific results of this paper are based in part on data obtained from the Chandra Data Archive: ObsID 13401, 16135, 16545, 19581, 19582, 19583, 20630, 20631, 20634, 20635, 20636, and 20797. ALMA is a partnership of ESO (representing its member states), NSF (USA) and NINS (Japan), together with NRC (Canada), MOST and ASIAA (Taiwan), and KASI (Republic of Korea), in cooperation with the Republic of Chile. The Joint ALMA Observatory is operated by ESO, AUI/NRAO and NAOJ. The National Radio Astronomy Observatory is a facility of the National Science Foundation operated under cooperative agreement by Associated Universities, Inc. This work was supported by Japan Society for the Promotion of Science (JSPS) KAKENHI Grant Numbers JP15H03639 (TA), JP15H05892 (MO), JP15K17614 (TA), JP17H01110 (TA), JP17H06130 (KK, RK), JP18K03693 (MO), JP18K03703 (ST), and JP18K03704 (TK), by the NAOJ ALMA Scientific Research Grant Number 2017-06B (KK), by the Ministry of Science and Technology of Taiwan (grant MOST 106-2628-M-001-003-MY3), and by Academia Sinica (grant AS-IA-107-M01).

References

Akahori, T., et al. 2019, PASJ, submitted
Anders, E., & Grevesse, N. 1989, Geochim. Cosmochim. Acta, 53, 197
Arnaud, K. A. 1996, ASP Conf. Ser., 101, Astronomical Data Analysis Software and Systems V, ed. G. H. Jacoby & J. Barnes (San Francisco: ASP), 17
Arnaud, M., Pratt, G. W., Piffaretti, R., Böhringer, H., Croston, J. H., & Pointecouteau, E. 2010, A&A, 517, A92
Asplund, M., Grevesse, N., Sauval, A. J., & Scott, P. 2009, ARA&A, 47, 481
Bartalucci, I., Mazzotta, P., Bourdin, H., & Vikhlinin, A. 2014, A&A, 566, A25
Basu, K., et al. 2010, A&A, 519, A29
Carlstrom, J. E. 2011, PASP, 123, 568
Cornwell, T. J. 2008, IEEE J. Selected Topics in Signal Processing, 2, 793
Fabian, A. C. 1994, ARA&A, 32, 277
Fabian, A. C. 2012, ARA&A, 50, 455
Fruscione, A., et al. 2006, Proc. SPIE, 6270, 62701V
Itoh, N., & Nozawa, S. 2004, A&A, 417, 827
Kaastra, J. S., Mewe, R., & Nieuwenhuijzen, H. 1996, in UV and X-ray Spectroscopy of Astrophysical and Laboratory Plasmas, ed. K. Yamashita & T. Watanabe (Tokyo: Universal Academy Press), 411
Kalberla, P. M. W., Burton, W. B., Hartmann, D., Arnal, E. M., Bajaja, E., Morras, R., & Pöppel, W. G. L. 2005, A&A, 440, 775
Kitayama, T., et al. 2016, PASJ, 68, 88
Kitayama, T., Komatsu, E., Ota, N., Kuwabara, T., Suto, Y., Yoshikawa, K., Hattori, M., & Matsuo, H. 2004, PASJ, 56, 17
McDonald, M., et al. 2012, Nature, 488, 349
McDonald, M., et al. 2014a, ApJ, 784, 18
McDonald, M., et al. 2014b, ApJ, 794, 67
McDonald, M., et al. 2015, ApJ, 811, 111
McDonald, M., et al. 2019, ApJ, 885, 63
McDonald, M., Benson, B., Veilleux, S., Bautz, M. W., & Reichardt, C. L. 2013, ApJ, 765, L37
McMullin, J. P., Waters, B., Schiebel, D., Young, W., & Golap, K. 2007, ASP Conf. Ser., 376, Astronomical Data Analysis Software

Downloaded from https://academic.oup.com/pasj/article/72/2/33/5803376 by University of Tsukuba user on 07 October 2021

and Systems XVI, ed. R. A. Shaw et al. (San Francisco: ASP), 127
McNamara, B. R., & Nulsen, P. E. J. 2007, ARA&A, 45, 117
Mittal, R., McDonald, M., Whelan, J. T., & Bruzual, G. 2017, MNRAS, 465, 3143
Nagai, D., Kravtsov, A. V., & Vikhlinin, A. 2007, ApJ, 668, 1
Nord, M., et al. 2009, A&A, 506, 623
Pinto, C., Bambic, C. J., Sanders, J. S., Fabian, A. C., McDonald, M., Russell, H. R., Liu, H., & Reynolds, C. S. 2018, MNRAS, 480, 4113
Planck Collaboration 2013, A&A, 550, A131
Planck Collaboration 2018, arXiv:1807.06209
Plucinsky, P. P., Bogdan, A., Marshall, H. L., & Tice, N. W. 2018, Proc. SPIE 10699, 106996B
Reichert, A., Böhringer, H., Fassbender, R., & Mühlegger, M. 2011, A&A, 535, A4
Rich, J. W., de Blok, W. J. G., Cornwell, T. J., Brinks, E., Walter, F., Bagetakos, I., & Kennicutt, R. C. 2008, AJ, 136, 2897
Russell, H. R., et al. 2017, ApJ, 836, 130
Sanders, J. S. 2006, MNRAS, 371, 829
Schure, K. M., Kosenko, D., Kaastra, J. S., Keppens, R., & Vink, J. 2009, A&A, 508, 751
Steeb, J.-W., & Rau, U. 2019, CASA Memo, 9
Sunyaev, R. A., & Zel'dovich, Ya. B. 1970, Comments Astrophys. Space Phys., 2, 66
Sunyaev, R. A., & Zel'dovich, Ya. B. 1972, Comments Astrophys. Space Phys., 4, 173
Tozzi, P., et al. 2015, A&A, 580, A6
Ueda, S., et al. 2018, ApJ, 866, 48
Ueda, S., Hayashida, K., Anabuki, N., Nakajima, H., Koyama, K., & Tsunemi, H. 2013, ApJ, 778, 33
Verde, L., Treu, T., & Riess, A. G. 2019, Nature Astron., 3, 891
Vikhlinin, A., Kravtsov, A., Forman, W., Jones, C., Markevitch, M., Murray, S. S., & Van Speybroeck, L. 2006, ApJ, 640, 691
Voit, G. M. 2011, ApJ, 740, 28
Voit, G. M., Kay, S. T., & Bryan, G. L. 2005, MNRAS, 364, 909
Williamson, R., et al. 2011, ApJ, 738, 139

Downloaded from https://academic.oup.com/pasj/article/72/2/33/5803376 by University of Tsukuba user on 07 October 2021